

PCCP

Accepted Manuscript



This is an *Accepted Manuscript*, which has been through the Royal Society of Chemistry peer review process and has been accepted for publication.

Accepted Manuscripts are published online shortly after acceptance, before technical editing, formatting and proof reading. Using this free service, authors can make their results available to the community, in citable form, before we publish the edited article. We will replace this *Accepted Manuscript* with the edited and formatted *Advance Article* as soon as it is available.

You can find more information about *Accepted Manuscripts* in the [Information for Authors](#).

Please note that technical editing may introduce minor changes to the text and/or graphics, which may alter content. The journal's standard [Terms & Conditions](#) and the [Ethical guidelines](#) still apply. In no event shall the Royal Society of Chemistry be held responsible for any errors or omissions in this *Accepted Manuscript* or any consequences arising from the use of any information it contains.

Modelling the chemistry of Mn-doped MgO for bulk and (100) surfaces †

Andrew J. Logsdail^{a,b,e}, Christopher A. Downing^{a,c}, Thomas W. Keal^c, Paul Sherwood^c, Alexey A. Sokol^a and C. Richard A. Catlow^{*a,b,d}

Received Xth XXXXXXXXXX 20XX, Accepted Xth XXXXXXXXXX 20XX

First published on the web Xth XXXXXXXXXX 200X

DOI: 10.1039/b000000x

We have investigated the energetic properties of Mn-doped MgO bulk and (100) surfaces using QM/MM computational methods, calculating the formation energy for doped systems, as well as for surface defects, and the subsequent effect on chemical reactivity. Low-concentration Mn doping is endothermic for isovalent species in the bulk but exothermic for higher oxidation states under p-type conditions, as favourably compensated by electrons going to the Fermi level rather than cation vacancies. The highest occupied dopant Mn 3d states are positioned in the MgO band gap, about 4.2 eV below the vacuum level. Surface Mn-doping is more favourable than subsurface doping, and marginally exothermic on a (100) surface at high O₂ pressures. For both types of isovalent Mn-doped (100) surfaces, the formation energy for catalytically important oxygen defects is less than for pristine MgO, with F⁰ and F²⁺-centres favoured in n- and p-type conditions, respectively. In addition, F⁺-centres are stabilised by favourable exchange coupling between the Mn 3d states and the vacancy-localised electrons, as verified through calculation of the vertical ionisation potential. The adsorption of CO₂ on to the pristine and defective (100) surface is used as a probe of chemical reactivity, with isovalent subsurface Mn dopants implicitly affecting reactivity whereas isovalent surface-positioned Mn strongly alters the chemical interactions between the substrate and adsorbate. The differing chemical reactivity, when compared to pristine MgO, justifies further detailed investigations for more varied oxidation states and dopant species.

1 Introduction

Rocksalt alkali-earth oxides, such as CaO and MgO, are amongst the materials currently under investigation for adsorbing and catalysing the transformation of CO₂.^{1,2} The bulk and surface structures of these oxides have been extensively studied,^{3–5} owing both to the simplicity of the rocksalt geometry and also the high degree of ionicity, which gives rise to a relatively simple electronic structure.^{6,7} Additionally, basic oxides such as MgO are popular as catalyst support materials but have displayed interesting reactivity when dopants or defects are included,⁸ which opens up the possibility for their use as catalysts in their own right.^{3,9–12} Whilst the surface chemistry and reactivity of MgO is well studied, only recently

have investigations begun to show the potential of MnO in areas such as photocatalytic water splitting and CO₂ reduction applications when alloyed with ZnO,¹³ and the (100) MnO surface has also been considered for CO₂ adsorption as part of a systematic study of transition metal monoxides.¹⁴ The doping of rocksalt alkali-earth oxides with transition metals has proven to result in novel physical and catalytic properties^{15–17} and thus the catalytic reactivity of MnO, coupled with the stability of the MgO surface, makes Mn-doped MgO an appealing material when designing novel catalytic systems. Furthermore, Mn²⁺ can directly replace Mg²⁺ without significant structural distortion as the ions are roughly equivalent in size; Mn-doped MgO is therefore structurally very similar to pristine MgO but can be differing in chemical reactivity, due to the range of stable oxidation states for the Mn-dopant.^{18–21}

Previous studies on Mn-doped MgO, which we refer to henceforth as Mn-MgO, have focused on the enthalpies of mixing for MgO and MnO^{22–24}, which are generally positive (endothermic) and small (< 0.1 eV), as well as formation energies and defect properties for low concentration isovalent Mn-dopants with the aim of finding a dilute magnetic semiconductor (DMS) for use in spintronic applications.^{25–31} In particular, recent work has emphasised understanding the consequences of increasing Mn concentration and the coupling

† Electronic Supplementary Information (ESI) available: Additional data table with CO₂ adsorption energies for pristine Mn-MgO (100) surfaces. See DOI: 10.1039/b000000x/

^a Kathleen Lonsdale Materials Chemistry, Department of Chemistry, University College London, 20 Gordon Street, London, WC1H 0AJ, United Kingdom

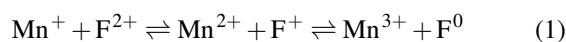
^b Cardiff Catalysis Institute, School of Chemistry, Cardiff University, Cardiff, CF10 3AT, United Kingdom

^c Scientific Computing Department, STFC Daresbury Laboratory, Daresbury, Warrington, WA4 4AD, United Kingdom

^d UK Catalysis Hub, Research Complex at Harwell, Science and Technology Facilities Council Rutherford Appleton Laboratory, Harwell Science and Innovation Campus, Oxon, OX11 0QX, United Kingdom

^e Tel: +44 (0)20 7679 0312 ; E-mail: a.logsdail@ucl.ac.uk

between extrinsic and intrinsic defects for both bulk and discrete systems. Experimental and modelling work by Azzaza *et al.* has shown that increasing Mn content in MgO decreases the band gap and Curie temperature for dopant concentrations of 5 to 40%, and magnetic interaction between isovalent Mn dopants and oxygen vacancies is postulated as influential to the stability.²⁷ Panigrahi *et al.* showed via computation that isovalent Mn dopants are favourably positioned at (100) surfaces, rather than in the bulk, for an MgO slab model, and that short-range anti-parallel coupling between multiple Mn dopants is favoured in the absence of intrinsic defects;³⁰ they then additionally highlighted that exchange coupling between isovalent Mn dopants and oxygen vacancies was also energetically favourable for bulk and surface models.^{30,31} MgO surfaces are commonly host to high concentrations of oxygen defects^{8,32} and, in the presence of the Mn 3d dopants, strong hybridisation between the Mn 3d and O 2p bands³⁰ means that novel chemistry of the material could be driven by the interchange of electrons between the redox active manganese atom and oxygen vacancy e.g.:



The equilibrium in Equation 1 depends on both the ionisation potential and electron affinity for the F-centres and Mn^+ , Mn^{2+} and Mn^{3+} cations within the octahedrally coordinated lattice, with the lowest energy configuration taking precedence. For clarity, in Kröger-Vink notation³³ the F^0 , F^+ and F^{2+} -centres are denoted as $\text{V}_{\text{O}}^{\times}$, $\text{V}_{\text{O}}^{\bullet}$ and $\text{V}_{\text{O}}^{\bullet\bullet}$, respectively, and the equivalent equations are:



In this work we present high-level computational simulations of Mn-MgO in order to elucidate the energetic and electronic properties of bulk- and surface-doped Mn-MgO. Firstly, formation energies of the Mn-doped systems are presented for a range of oxidation states and then complemented by calculations that highlight the role of electron-spin coupling between the Mn 3d states and electrons trapped at intrinsic vacancies such as surface F-centres. The strength of this spin-coupling is then used to help explain the interaction between a CO_2 adsorbate and the Mn-MgO (100) surface, both with and without F-centres.

2 Computational Methodology

Calculations were performed using the hybrid quantum mechanical and molecular mechanical (QM/MM) embedded-cluster methodology, as has previously proven accurate for modelling the bulk and surface chemistry of MgO.^{8,34-43} Our chosen QM/MM implementation is the software package

Coul. & Spring	q_{core}	q_{shell}	k_2	k_4
Mg	0.415	1.585	361.60	0.0
Mn	-1.420	3.420	95.00	0.0
O	1.000	-3.000	54.76	0.0
Buck.	A	ρ	C	r_c
$\text{Mg}_{\text{shell}}-\text{O}_{\text{shell}}$	1428.5	0.2945	0.0	12.0
$\text{Mn}_{\text{shell}}-\text{O}_{\text{shell}}$	1007.4	0.3262	0.0	12.0
$\text{O}_{\text{shell}}-\text{O}_{\text{shell}}$	22764.3	0.1490	23.0	12.0

Table 1 Forcefield parameters for the Mn-MgO calculations. Coul. and Buck. are abbreviations for Coulomb and Buckingham, respectively. The parameters are the core charge (q_{core} , in e), the shell charge (q_{shell} , in e), the spring constants (k_2 and k_4 , in $\text{eV}\text{\AA}^{-2}$ and $\text{eV}\text{\AA}^{-4}$, respectively), the unitless Buckingham potential parameters A , ρ and C , and the cutoff for the potential (r_c) in \AA .

ChemShell,⁴⁴⁻⁴⁶ with QM and MM energy evaluations performed with the NWChem⁴⁷ and GULP⁴⁸⁻⁵⁰ software packages, respectively, and geometry optimisation was performed using the DL-FIND software routines.⁴⁵

For the QM calculations, density functional theory (DFT) was used with the B3LYP⁵¹⁻⁵³ and B97-3⁵⁴ exchange-correlation (XC) functionals. Results obtained using B3LYP provide a direct comparison with previous work for MgO,⁴² while B97-3 provides comparison with an XC functional that was fitted to a more extensive set of molecular thermochemical data. A Def2 triple-zeta valence plus polarisation (TZVP) basis set⁵⁵ was used for all atoms except Mn, where a Stuttgart/Dresden relativistic small-core effective core potential (ECP) was used with a complementing modified basis set:⁵⁶ the most diffuse functions were removed to prevent the artificial spreading of charge density outside the QM region. Large core ECPs⁵⁷ for Mg^{2+} ions were placed on cations at the border of the QM region, representing the QM/MM boundary. The redox-active Mn dopant can adopt different energetically-competitive spin configurations, particularly when neighbouring an unpaired electron on an oxygen vacancy (F^+), and thus the spin-states were explicitly checked. High-spin (HS) configurations were energetically favoured for defect-free systems, which preserves the unpaired Mn d^5 configuration in Mn-MgO in agreement with previous calculations.^{26,28} For pure MgO, a closed-shell configuration was always preferable. Unless otherwise stated, all calculations use these configurations.

The MM energy is calculated using a polarisable interatomic forcefield with Coulomb ($E_{\text{MM}}^{\text{Coul}}$), Buckingham ($E_{\text{MM}}^{\text{Buck}}$) and spring ($E_{\text{MM}}^{\text{spring}}$) terms that are defined as:⁴⁹

$$E_{\text{MM},ij}^{\text{Coul}} = \frac{q_i q_j}{r_{ij}} \quad (3)$$

$$E_{\text{MM},ij}^{\text{Buck}} = Ae^{\left(\frac{-r_{ij}}{\rho}\right)} - \frac{C_6}{r_{ij}^6} \quad (4)$$

$$E_{\text{MM},ij}^{\text{spring}} = \frac{1}{2}k_2r_{ij}^2 + \frac{1}{24}k_4r_{ij}^4 \quad (5)$$

between two centres with indices i and j , separated by a distance of r_{ij} . The parameters are the charge (q , in e), the spring constants (k_2 and k_4 , in $\text{eV}\text{\AA}^{-2}$ and $\text{eV}\text{\AA}^{-4}$, respectively) and the unitless Buckingham potential parameters A , ρ and C . The parameterisations we have used, which are presented in Table 1, are slightly modified versions of those derived by Lewis & Catlow:⁵⁸ the cut-off radius has been extended from 6 to 12 \AA and the $\text{O}_{\text{shell}}-\text{O}_{\text{shell}}$ interaction tuned in order to reproduce accurately the dielectric constants of MgO, with polarisable shells included on cations as well as anions. No additional potential terms were included to account for the interactions of the CO_2 adsorbates with the surface as the closest MM atoms were at least 5 \AA away.

A spherical or hemispherical QM/MM cluster was used for bulk and surface models, respectively, with a total radius of 30 \AA centred on either an oxygen atom or vacancy. The central QM region contained a total of 33 atoms for the bulk and from 22 to 26 atoms for the surface (e.g. Figure 2); this setup previously produced accurate results for MgO.⁴² The radius of the active MM region was set to 15 \AA as atoms beyond this distance did not move during previous geometry optimisations.⁴² This partitioning meant that ~ 1500 (~ 850) atoms underwent ionic relaxation in our bulk (slab) models, with atoms beyond 15 \AA fixed in their lattice positions. The lattice constant was obtained for MgO using GULP and the forcefield of choice. Once cut, the surface clusters were oriented such that the x - and y -axes are in the plane of the surface, and the z -axis is perpendicular to the surface.

The total energy of the system is defined additively as:

$$E_{\text{Total}} = E_{\text{QM}} + E_{\text{MM}} + E_{\text{Jost}} \quad (6)$$

where E_{MM} and E_{QM} are the energies of the MM and QM regions, respectively, and E_{Jost} is the Jost correction, necessary due to the finite size of the relaxed region of the QM/MM model when dealing with charged defects, thus incorporating long range effects through a dielectric medium term. For the bulk, E_{Jost} is:⁵⁹

$$E_{\text{Jost}}^{\text{bulk}} = -\frac{Q^2}{2R} \left(1 - \frac{1}{\epsilon}\right) \quad (7)$$

where Q denotes the total charge of any defect in the system, R is the radius of the relaxed region in a_0 and ϵ is the dielectric constant of the material, which in this case is MgO. For a surface, E_{Jost} is:⁵⁹

$$E_{\text{Jost}}^{\text{surf}} = -\frac{Q^2(\epsilon - 1)}{2R(\epsilon + 1)}. \quad (8)$$

We have used the static (ϵ_0) and high-frequency (ϵ_∞) dielectric constants when calculating E_{Jost} for adiabatic and instantaneous processes, respectively. The MM forcefield was used to calculate ϵ_0 (9.7033) and ϵ_∞ (3.01584), with both values matching closely the available experimental literature for static (9.65, 9.8) and optical (2.95) dielectric constants.⁶⁰

3 Mn-doped MgO Bulk

In order to test and validate our QM/MM model, we calculated the energy required to replace Mg with an Mn atom in MgO. The reaction scheme of this substitution is:



where (ref) indicates a reference state. Thus, the formation energy, $E_f(\text{Mn-MgO})$, can be written as:

$$E_f(\text{Mn-MgO}) = E(\text{Mn-MgO}) - E(\text{MgO}) + E(\text{Mg}) - E(\text{Mn}) + q\epsilon_f, \quad (10)$$

where $E(\text{Mn-MgO})$, $E(\text{MgO})$, $E(\text{Mg})$ and $E(\text{Mn})$ are the energy of the doped Mn-MgO, pristine MgO, Mg reference and Mn reference, respectively, and the charge of non-isovalent systems are accounted through the inclusion of the final $q\epsilon_f$ term, where q is the formal charge of the defect, i.e. $\text{Mn}^{(2+q)+}$, and ϵ_f is the Fermi level of the system. An alternative sink for compensating electrons is cationic vacancies^{61,62}, which we have considered as doubly-charged Mg vacancies (V_{Mg}'') formed as:



Considering our Mn-doped systems, $\text{Mg}_{\text{at}}^{\bullet\bullet}$ can be replaced with Mg_{at}^x as the holes instead localise on the extrinsic defects, with substitution in the place of ϵ_f in Equation 10 giving:

$$E_f(\text{Mn-MgO}) = E(\text{Mn-MgO}) - E(\text{MgO}) + E(\text{Mg}) - E(\text{Mn}) + \frac{q}{2}\{E(\text{Mg}) + E(\text{V}_{\text{Mg}}'') - E(\text{MgO})\}, \quad (12)$$

where q is again the formal charge of the Mn-dopant in MgO and a factor of $\frac{1}{2}$ appears due to the double charge on the Mg vacancy. In all cases, the energy of the Mg reference state is:

$$E(\text{Mg}) = E(\text{Mg}_{\text{at}}) + \mu(\text{Mg}), \quad (13)$$

where $E(\text{Mg}_{\text{at}})$ is the calculated energy of the gas-phase atom and $\mu(\text{Mg})$ is the chemical potential of Mg, with $E(\text{Mn})$ calculated similarly. $E(\text{Mg}_{\text{at}})$ and $E(\text{Mn}_{\text{at}})$ were calculated as $E(\text{Mg}_{\text{at}}^{2+})$ and $E(\text{Mn}_{\text{at}}^{2+})$ minus the respective 1st and 2nd experimental ionisation energies for each element, as successfully applied previously for embedded-cluster calculations

	B3LYP	B97-3	MM
Mn _{bulk}	2.73 (0.49)	2.55 (0.31)	-(0.23)
Mn _{sub}	2.67 (0.43)	2.53 (0.28)	-(0.23)
Mn _{surf}	2.16 (-0.08)	2.00 (-0.24)	-(-0.35)
	5.354 (516.566)		

Table 2 $E_f(\text{Mn-MgO})$, in eV, for isovalent bulk (Mn_{bulk}), surface (Mn_{surf}) and subsurface (Mn_{sub}) sites as calculated for environments with low (*high*) $p(\text{O}_2)$ with the B3LYP and B97-3 XC functionals. For reference, $E_f(\text{Mn-MgO})$ for an Mn-dopant in an infinitely dilute MgO environment at high $p(\text{O}_2)$, as calculated using the presented MM forcefields, is also given. For $E_f(\text{Mn-MgO})$ relative to the gas phase atoms, one can subtract $\mu(\text{Mg}) - \mu(\text{Mn})$ from these values. A HS configuration (sextuplet multiplicity) was energetically preferred for Mn-MgO in all DFT calculations.

with edited basis sets.⁶³ $\mu(\text{Mg})$ and $\mu(\text{Mn})$ were derived using a Born-Haber cycle and literature values for energetic processes.⁶⁴

Mg(s) and Mn(s) are the reference states at low oxygen partial pressure, $p(\text{O}_2)$, and thus their vaporisation enthalpies of 143.38 and 279.58 kJ mol⁻¹ are used to derive $\mu(\text{Mg}) - \mu(\text{Mn}) = 136.2$ kJ mol⁻¹ (1.41 eV). In a physical sense, a positive value means the stronger bonding in the Mn(s) reactant would inhibit the reaction. In contrast, for high $p(\text{O}_2)$ the reference states are MgO (s) and MnO (s), respectively. In this case, the formation enthalpy for MgO (-601.6 kJ mol⁻¹) and MnO (-385.2 kJ mol⁻¹) are combined with the values above to give $\mu(\text{Mg}) - \mu(\text{Mn}) = -80.2$ kJ mol⁻¹ (-0.83 eV), with the negative value indicating favourability for the MgO product over the MnO reactant.

Our results for isovalent E_f^{bulk} (Mn-MgO) are presented in Table 2. The formation of Mn-dopants at low and high $p(\text{O}_2)$ are endothermic, with energies of 2.73 (2.55) and 0.49 (0.31) eV, respectively, for the B3LYP (B97-3) XC functional. Our high $p(\text{O}_2)$ results match previous work by Konigstein *et al.* and Heath *et al.* for the enthalpies of mixing (ΔH_{mix}) of MgO and MnO: 12.5 % MnO in MgO was found to be endothermic by 0.03 and 0.05-0.06 eV at the GULP and Hartree-Fock levels of theory, respectively,^{22,24} in good agreement with experiment (0.02 eV).²³ We believe that ΔH_{mix} (MgO/MnO) is lower than for our results due to the relaxation of the bulk lattice constants in this previous work;²² an effect that is not included in our calculations. Interestingly, all of these results are contrary to the Mn-doping DFT calculations of Panigrahi *et al.*³⁰ where results using the generalised-gradient approximation⁶⁵ give E_f^{bulk} (Mn-MgO) = -0.1 eV for a 64-atom unit cell, relative to atomic reference states, and adjustment for a high $p(\text{O}_2)$ environment gives $E_f(\text{Mn-MgO}) = -0.93$ eV, which is surprisingly exothermic.

Structural analysis of the B3LYP calculation shows that the

	q	$\epsilon_f = 0$ eV	$\epsilon_f = \text{VBM}$	
Mn _{bulk}	0	0.49 (0.31)	0.49 (0.31)	
	1	3.10 (3.11)	-3.18 (-3.40)	
	2	7.01 (7.23)	-5.53 (-5.79)	
	3	13.15 (13.49)	-5.67 (-6.03)	
	1 ^a	0.87 (0.68)	0.87 (0.68)	
	2 ^a	2.55 (2.37)	2.55 (2.37)	
	3 ^a	6.45 (6.20)	6.45 (6.20)	
	Mn _{sub}	0	0.43 (0.28)	0.43 (0.28)
		1	3.00 (3.00)	-3.15 (-3.40)
2		7.13 (7.37)	-5.17 (-5.42)	
3		13.67 (13.95)	-4.78 (-5.23)	
1 ^a		0.76 (0.58)	0.76 (0.58)	
2 ^a		2.67 (2.50)	2.67 (2.50)	
3 ^a		6.98 (6.65)	6.98 (6.65)	
Mn _{surf}		0	-0.08 (-0.24)	-0.08 (-0.24)
		1	2.54 (2.56)	-3.60 (-3.83)
	2	7.54 (7.72)	-4.76 (-5.06)	
	3	14.16 (14.32)	-4.29 (-4.85)	
	1 ^a	0.31 (0.13)	0.31 (0.13)	
	2 ^a	3.08 (2.86)	3.08 (2.86)	
	3 ^a	7.46 (7.03)	7.46 (7.03)	

Table 3 $E_f(\text{Mn-MgO})$, in eV, for bulk (Mn_{bulk}), surface (Mn_{surf}) and subsurface (Mn_{sub}) sites as calculated with the B3LYP (B97-3) XC functional at high $p(\text{O}_2)$ for varying charge (q) and position of ϵ_f , with the latter ranging between vacuum (0 eV) and the valence band maximum (VBM). Values of q marked with ^a have been compensated by cation vacancies (Equation 12), with all other values compensated by the use of the Fermi level (Equation 10).

Mn-O bond length in the doped system is 2.18 Å, which is an extension of the Mg-O bond length (2.12 Å); identical extensions of the metal-oxygen bond occurs when the XC is B97-3. Our results are in broad agreement with experimental lattice parameters for MgO (2.11 Å) and MnO (2.22 Å),⁶⁴ and with previous computational reports for isolated Mn dopants in MgO, which give an Mn-O bond distance of ~ 2.1 Å.³⁰

Figure 1 illustrates the formation energy for Mn dopants of differing charge states in MgO, in the range $0 \leq q \leq 5$, within the limits of ϵ_f . This graph can be considered as a guide to the favoured oxidation state of an Mn-dopant in either p- or n-type conditions. The lower bound for ϵ_f is the valence band maximum (VBM), which we position as the negative of the vertical ionisation potential (VIP) for MgO. QM/MM allows us to calculate the VIP for MgO as 6.27 (6.51) eV for the B3LYP (B97-3) XC functional using the ΔSCF technique,⁶⁶ which is a slight underestimate of experiment (7.16 eV)⁶⁷ and lower than our previous estimates using XC functionals tuned

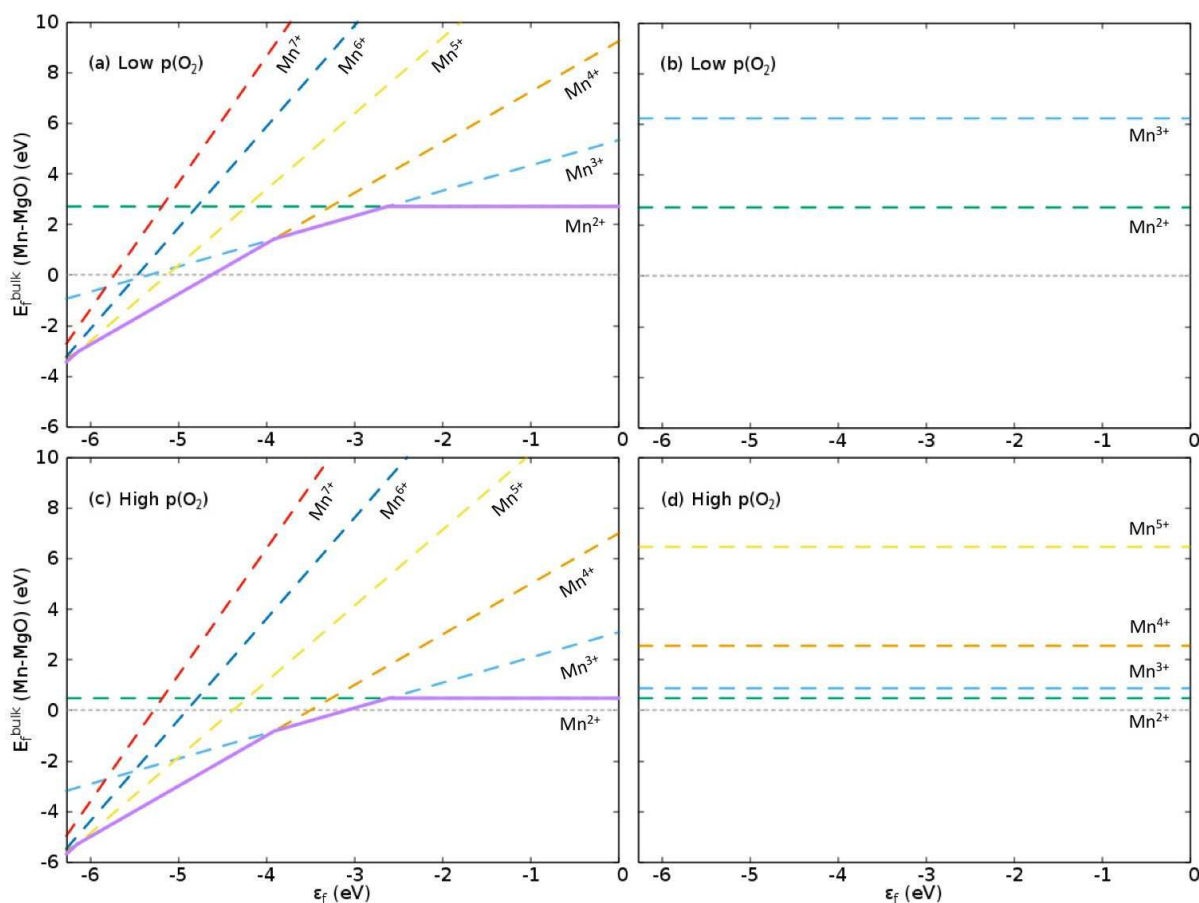


Fig. 1 E_f for bulk Mn dopants in MgO when using the B3LYP XC functional at (a,b) low and (c,d) high $p(\text{O}_2)$, with ϵ_f ranging from the VBM (-6.27 eV) through to vacuum level (0 eV). Figures (a) and (c) show E_f as compensated by electrons transferring to the Fermi level, ϵ_f , as calculated with Equation 10 whilst Figures (b) and (d) show E_f as compensated by cation (Mg) vacancies (Equation 12). Dashed green, aqua, gold, yellow, navy blue and red lines show E_f when the defect charge is respectively $q=0, 1, 2, 3, 4$ and 5 , i.e. ranging from Mn^{2+} to Mn^{7+} as $\text{Mn}_{\text{Mg}}^{\times}$, $\text{Mn}_{\text{Mg}}^{\bullet}$, $\text{Mn}_{\text{Mg}}^{\bullet\bullet}$, $\text{Mn}_{\text{Mg}}^{\bullet\bullet\bullet}$, $\text{Mn}_{\text{Mg}}^{\bullet\bullet\bullet\bullet}$ and $\text{Mn}_{\text{Mg}}^{\bullet\bullet\bullet\bullet\bullet}$, respectively. The overall preferred defect charge as a function of ϵ_f , which is found to be compensated by the Fermi level in all cases, is given as a solid purple line in Figures (a) and (c).

for bulk materials (PBE0: 6.89 eV; PBESol0: 6.97 eV).⁶ The upper bound for ϵ_f would typically be the conduction band minimum (CBM) but the band gap of MgO (7.83 eV)⁶⁸ is greater than the VIP, which means the conduction band is actually above the vacuum level. As electrons would not favour going into a CBM with a positive energy, the vacuum level (0 eV) becomes the upper bound for ϵ_f . Comparison of the Mulliken analysis for the bulk MgO and $[\text{MgO}]^+$ models shows that the electrons are ionised from the 2p states of the central oxygen, though the remaining electron hole is delocalised over neighbouring atoms as also previously documented for MgO surfaces.³⁵ In addition to these observations, we also calculated the 1st and 2nd VIPs for $\text{Mn}_{\text{bulk}}\text{-MgO}$ to be 4.27 (4.38) and 5.62 (5.86) eV, respectively, which means that the highest occupied Mn 3d states are positioned in the bandgap, in agreement with previous reports^{25–27}. For higher order VIPs,

the Mn 3d states hybridise with the O 2p states in the energy range of -8 to -11 eV to form ill-defined resonance states.

The graphs for Fermi level-compensated Mn-dopants in (a) low and (c) high $p(\text{O}_2)$ in Figure 1 are clear translations of each other, with both showing that a like-for-like replacement of Mg with Mn is preferred when ϵ_f is close to 0 eV. Reducing ϵ_f results in a shift in favourability towards higher oxidation states, which may be attributed to factors such as the stability of Mn in 3+, 4+ and 5+ oxidation states; in experiment the position of ϵ_f would be strongly dependent on factors such as the dopant concentration. For low $p(\text{O}_2)$, E_f for Mn^{4+} is exothermic below $\epsilon_f = -4.63$ eV, and for high $p(\text{O}_2)$ the formation of Mn^{3+} and Mn^{4+} is exothermic below $\epsilon_f = -3.10$ and -3.51 eV, respectively, with formation of higher oxidation states also exothermic at lower ϵ_f in both cases: Mn^{5+} is the most favourable dopant state in both environments in the range of

ϵ_f from -6.13 to -6.27 eV. We note from graphs (b) and (d) in Figure 1, and Table 3, that using Mg vacancies as compensating defects results in higher formation energies than using the Fermi level, though the Mn^{3+} defect is competitive with the isovalent defect at high $p(\text{O}_2)$, differing by 0.38 eV. This observation is general to our calculations for B3LYP and B97-3, as shown in Table 3, with only the former plotted in Figure 1 and discussed in detail here: the difference in E_f for isovalent (2+) and 3+ Mn-dopants when using the latter XC functional is also 0.38 eV.

In general, it is noted that Mn-doping is exothermic in p-type conditions, both at low and high $p(\text{O}_2)$. As the dopant concentration increases the material will become more n-type due to the presence of Mn-defect states in the band gap, resulting in changes to the most stable Mn oxidation state: at $\epsilon_f = -4.27$ (-4.38) eV, Mn^{4+} is thermodynamically favoured. Lower oxidation states, such as isovalent Mn^{2+} , are endothermic in formation and would require n-type conditions during synthesis. Typically, n-type conditions are achieved by using low $p(\text{O}_2)$, which results in oxygen vacancies with defect states high in the band gap, as discussed further on; surface oxygen vacancies are also of interest for catalytic purposes, where the F-centres can play an important role in reactivity. Therefore, the material properties could be tuned with careful synthesis protocols.

Due to the similarity of our results thus far for the different XC functionals, only those acquired using the B3LYP XC functional will be discussed subsequently herein unless explicitly stated.

4 Mn-doped MgO (100) Surface

4.1 Position of Mn-dopant

As illustrated in Figure 2, two different QM/MM clusters were used for the Mn-MgO surfaces: (a) the Mn dopant positioned in the surface layer (Layer 1, L1), adjacent to the central oxygen; (b) the Mn dopant situated in the first subsurface layer (Layer 2, L2), directly beneath the central oxygen. Henceforth, these two configurations will be referred to as Mn_{surf} and Mn_{sub} , respectively. The Cartesian axes of the QM/MM cluster have been defined such that the xy -plane aligns with the surface-plane of the model; thus Mn_{sub} occupies the Mg lattice position $(0,0,z)$ and Mn_{surf} occupies the Mg lattice position $(x,0,0)$, with the primary oxygen lattice site (O_{5c} or F-centre) at $(0,0,0)$.

Our results, which are presented in Table 2 and 3, show that formation of isovalent Mn-doped surface layers is exothermic at high $p(\text{O}_2)$ when compensated using ϵ_f , whereas formation of subsurface dopants is very similar to bulk, being endothermic for all $p(\text{O}_2)$. With reduction of ϵ_f from 0 eV towards the VBM, higher oxidation states become more prefer-

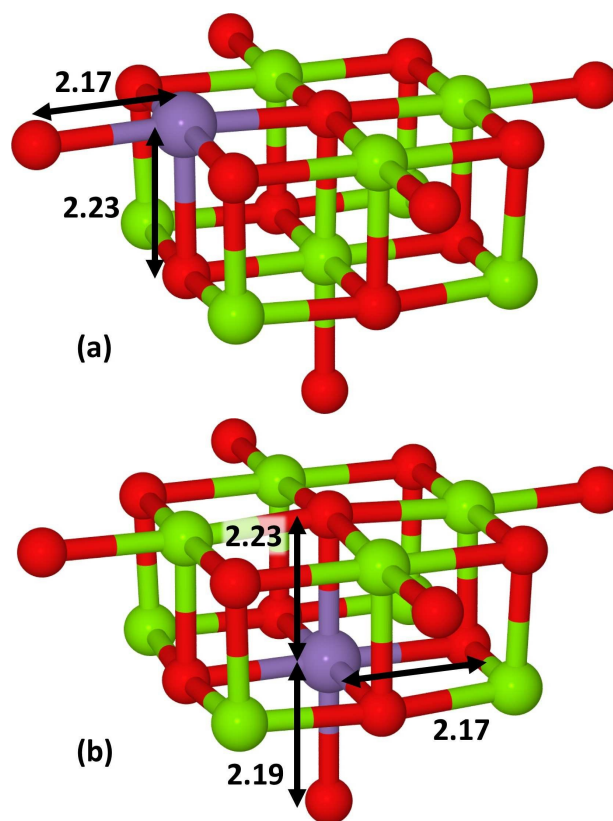


Fig. 2 QM cluster illustrating the Mn-dopant in (a) surface (Mn_{surf}) and (b) subsurface (Mn_{sub}) positions. O atoms are shown in red, Mg in green and Mn in purple. Bond lengths are given in Å.

able with Mn^{4+} the most stable at $\epsilon_f = \text{VBM}$. In contrast, cation-vacancy compensated defects remain endothermic (Table 3). Overall, Mn_{surf} is energetically favoured over Mn_{sub} (and Mn_{bulk}) for $q = 0$ and 1 as the electronic and structural flexibility of the surface minimises any strain induced by the discrepancy in radius between Mn and Mg (0.83 vs. 0.72 Å for 2+ cations, respectively).⁶⁹ In addition, at these charge states $E_f(\text{Mn}_{\text{surf}}) > E_f(\text{Mn}_{\text{bulk}})$, whereas $E_f(\text{Mn}_{\text{sub}}) \approx E_f(\text{Mn}_{\text{bulk}})$. We note that low-spin (LS) Mn^{2+} is in fact structurally smaller (0.67 Å) than HS Mn^{2+} ,⁶⁹ in octahedral coordination, but a half-filled d-shell with no degenerate occupancy (HS d^5) is energetically preferable, which also means no Jahn-Teller distortion is observed, in agreement with previous calculations.³⁰ For $q > 1$, it is apparent that long-distance bulk electrostatics are more important, with Mn^{5+} unstable with respect to Mn^{4+} at the surface and sub-surface yet preferred in the bulk.

On the un-doped MgO (100) surface, the Mg-O bond lengths are 2.12 Å in the xy -plane and the z -direction (L1 to L2). These bonds extend to 2.17 and 2.23 Å, respectively, for isovalent Mn_{surf} and the O- Mn_{surf} -O bond angles are 90.0° in the xy -plane but as low as 88.5° and 87.3° in the xz -

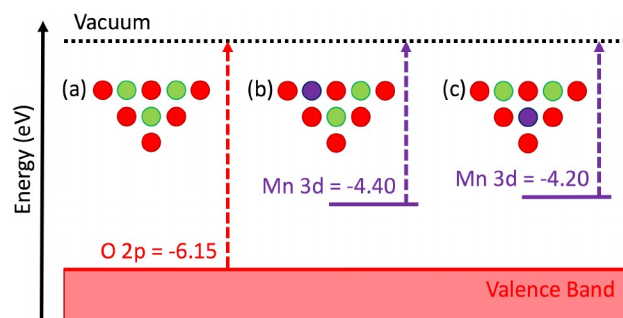


Fig. 3 Position of the surface valence band and defect states, relative to vacuum, for (a) MgO; (b) $\text{Mn}_{\text{surf}}\text{-MgO}$; and (c) $\text{Mn}_{\text{sub}}\text{-MgO}$ (100) surfaces. Red, green and purple circles represent O, Mg and Mn atoms, respectively. The colour scheme of the electronic transitions matches the origin of electrons for the vertical ionisation potential (VIP): the valence band is O 2p states and Mn 3d defect states are positioned in the band gap. The energies presented are calculated with the B3LYP XC functional, and the adiabatic ionisation potential (AIP) was calculated as 5.21, 2.62 and 2.56 eV for models (a), (b) and (c), respectively.

and yz -planes, respectively. The same bond angles are 91.6° for O-Mg-O, showing that the Mn dopants protrude outwards from the (100) surface whereas Mg withdraws inwards. For isovalent Mn_{sub} , Mn-O bond lengths are similarly extended to 2.17 Å in the xy -plane (L2-L2) and 2.22 (2.19) Å in the z -direction between L1 and L2 (L2 and Layer 3, L3), which is partly due to the relaxation of the surface oxygen atom outwards from the surface.⁷ For comparison, the same bonds for Mg-O in the pure surface are 2.18 and 2.07 Å for L1-L2 and L2-L3 interactions, which shows that the subsurface bond lengths increase by > 0.1 Å due to the Mn_{sub} -dopant. The O- Mn_{sub} -O bond angles within the xy -plane were maintained at 90.0° , similar to Mn_{surf} , whilst the elongation of the bonds in the z -direction, and upwards movement of Mn_{sub} , creates bond angles of up to 90.6° in the xz - and yz -planes between the L1 and L2 oxygens.

In order to place the VBM for the surface, as well as to ascertain which atoms contribute to the band edges and dopant states, we calculated the VIP and the adiabatic ionisation potential (AIP) of the pure and Mn-doped MgO (100) surfaces (Figure 3). For the MgO surface a VIP of 6.15 (6.39) eV is calculated with the B3LYP (B97-3) XC functional, which is in agreement with experiment (6.7 ± 0.4 eV)⁷⁰ though slightly lower than previous results from periodic DFT using XC functionals for bulk materials (6.52 - 6.57 eV)⁷ and QM/MM calculations with the B3LYP XC functional (6.46, ~ 6.5 eV)^{35,42}. We attribute this difference to the incomparable XC potentials used in the previous periodic DFT,⁷ the improvements in the MM forcefield and basis sets when compared to our own prior work⁴², and an absence of long-range corrections (E_{Jost}) in

the work of Sushko *et al.*³⁵; if we remove E_{Jost} from our calculations to match the latter work, the agreement between results improves with our VIP becoming 6.39 (6.63) eV for the B3LYP (B97-3) XC functional. In all cases, Mulliken analysis shows that the electron removed during ionisation is taken from the surface oxygen atoms, which shows that the VBM is O 2p states in agreement with well-developed theories of metal oxide band structures^{71,72}. We also calculated the AIP of MgO (100) to be 5.21 (5.23) eV, for the B3LYP (B97-3) XC functional, i.e. the relaxation of the nuclei around an electronic defect lowers the energy of the system by 0.94 (1.16) eV. The smaller VIP of the MgO surface when compared to bulk MgO is due to surface band bending, as we have discussed previously elsewhere.⁷

The VIP for Mn_{surf} - and $\text{Mn}_{\text{sub}}\text{-MgO}$ is calculated as 6.16 (6.41) and 6.14 (6.32) eV, respectively, when using the B3LYP (B97-3) XC functional with a septuplet multiplicity i.e. an ionised electron is removed from the O 2p orbitals, with the HS Mn d^5 configuration preserved. Unsurprisingly, these results match the VIP for the pure MgO surface, reported above, as the O 2p states contribute to the VBM. However, changing our setup to an intermediate quintet spin-configuration, with the ionised electron removed instead from the Mn 3d states to give an Mn d^4 electronic configuration, the VIP is 4.40 (4.63) and 4.20 (4.32) for the same dopant systems and XC functionals, respectively (Figure 3). The smaller VIP indicates that the highest occupied Mn 3d states are 1.76-1.94 eV above the O 2p states and thus in the band gap, matching the bulk systems (Section 3); the VIP of $\text{Mn}_{\text{sub}}\text{-MgO}$ is noted as being similar to the bulk, for which the VIP was calculated as 4.27 (4.38) eV. Mulliken analysis further confirms that the electrons are removed from the Mn 3d and O 2p orbitals for ionisation calculated with multiplicities of 5 and 7, respectively. Full localisation of the remaining holes is not achieved with ~ 0.55 and 0.2 e removed from the Mn and central O in each respective calculation; however the hole does fully localise on the Mn dopant after geometry relaxation. The AIP for the intermediate spin-state (IS) was calculated for Mn_{surf} - and $\text{Mn}_{\text{sub}}\text{-MgO}$ as 2.62 (2.81) and 2.56 (2.71) eV, respectively, using the B3LYP (B97-3) XC functional; the energetic relaxation of the nuclei, and localisation of the hole, results in significant stabilisation by 1.61 - 1.83 eV. In addition, higher-order 2nd and 3rd VIPs were calculated for Mn_{surf} - and $\text{Mn}_{\text{sub}}\text{-MgO}$: the results for $\text{Mn}_{\text{sub}}\text{-MgO}$ match those of Mn_{bulk} with the 2nd Mn 3d state at -6.02 eV, just above the VBM, whilst the 3rd Mn 3d state is in the valence band i.e. a resonance state. For $\text{Mn}_{\text{surf}}\text{-MgO}$, the 2nd Mn 3d state is already in the valence band, showing that the surface strongly stabilises the 3d states and indicating a reason for the improved stability of the Mn-dopant at the surface.

4.2 Oxygen Vacancy Formation

Oxygen vacancies that contain trapped electrons on the surface of a material, i.e. F-centres⁸, have previously been postulated as active sites for the conversion of CO₂ to CH₃OH on metal oxides, e.g. Cu/ZnO/Al₂O₃.^{46,73–77} As discussed in Section 3, the formation of such vacancies would require careful material preparation, however their presence would be beneficial for catalytic applications. Therefore, we have calculated the formation energies of oxygen vacancies at the Mn-MgO (100) surface, as presented in Table 4. The formation energy, $E_f(F^{q+})$, was calculated relative to the energy of the Mn-doped surface, $E(\text{Mn-MgO})$, and half an oxygen dimer, $\frac{1}{2}E(\text{O}_2)$:

$$E_f(F^{q+}) = E(F^{q+}\text{Mn-MgO}) - E(\text{Mn-MgO}) + \frac{1}{2}E(\text{O}_2) + q\varepsilon_f \quad (14)$$

As in Equation 10, ε_f is a variable that can vary between an upper limit of vacuum (0 eV) and a lower limit of the VBM, which we calculate as -6.15 (-6.39) eV for the B3LYP (B97-3) XC functional (Section 4.1). We discuss only $\varepsilon_f = 0$ eV in the text unless otherwise stated, as this is typical for a low $p(\text{O}_2)$ environment that would facilitate the formation of oxygen vacancies.

A closed-shell configuration is energetically favoured for a neutral F⁰-centre on the (100) surface, with both electrons occupying the oxygen vacancy, i.e. V_O^x, and the Mn²⁺ ion maintaining an open-shell d⁵ valence configuration. We denote this as intermediate-spin (IS), as a high-spin (HS) configuration would unpair the vacancy electrons and low-spin (LS) configuration would have the Mn d⁵ electrons paired together, both of which are energetically unfavourable. For Mn_{surf}- and Mn_{sub}-MgO, $E_f(F^0)$ is 6.14 (5.85) ± 0.02 eV for the B3LYP (B97-3) XC functional, which is ~0.4 eV lower than that of the pure MgO (100) surface,⁴² as shown in Figure 4.

In order to explore the effect of exchange coupling between the vacancy-trapped electrons and the Mn 3d-states for an F⁺-centre, we compare a parallel and anti-parallel alignment of the V_O and Mn 3d electrons. As can be seen in Table 4, IS (anti-parallel) alignment gives $E_f(F^+)$ of 7.64 eV for Mn_{surf}, with a very similar result for Mn_{sub}, and $E_f(F^+)$ is ~0.27 eV greater for the HS (parallel) configuration. The position of ε_f has significant effect on $E_f(F^+)$: when below -1.48 eV, $E_f(F^0) > E_f(F^+)$ for both Mn-doped surfaces. Additionally, $E_f(F^+\text{Mn-MgO})$ is at least 0.35 eV lower than $E_f(F^+\text{MgO})$, indicating that an Mn-dopant facilitates formation of an F⁺-centre (Figure 4).

Ionisation of a second electron to form an F²⁺-centre could also be from the oxygen vacancy or the Mn dopant, which could potentially lead to doubly-charged (a) Mn_{Mg}^{••} or (b) V_O^{••} defects, or alternatively (c) sharing of the holes between both

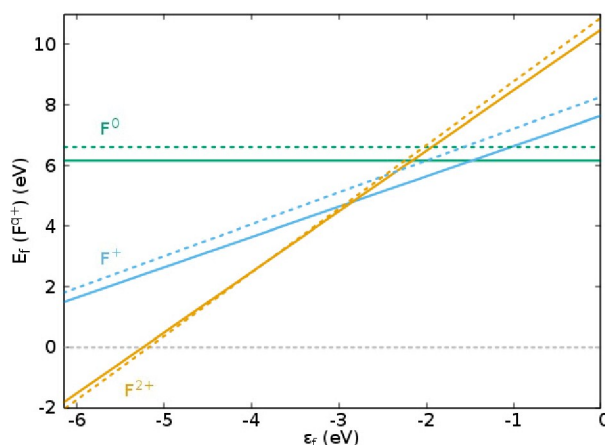


Fig. 4 E_f for F^{q+}-centres using the B3LYP XC functional, with solid lines representing Mn_{surf}-MgO, with ε_f ranging from the VBM (-6.15 eV) through to vacuum level (0 eV), and dashed lines representing the same defects on a pristine MgO surface, as calculated in Table 4 from the work of Downing *et al.*⁴² Dashed green, blue and yellow lines show E_f when the defect charge is $q=0, 1$ and 2 , respectively (i.e. F⁰, F⁺ and F²⁺).

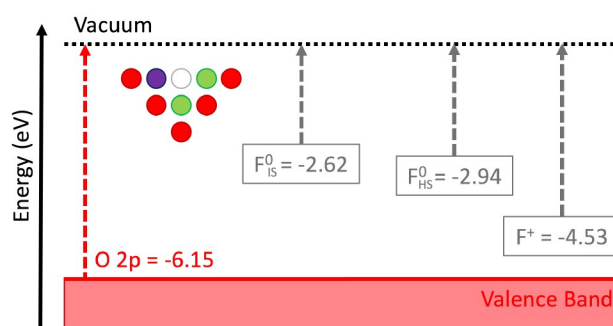


Fig. 5 Intrinsic defect levels, relative to vacuum, for F-centres on the Mn_{surf}-MgO (100) surface. The colour scheme of the atoms is the same as Figure 3, with an additional white circle to show an surface oxygen vacancy. The colour scheme of the electronic transitions matches the origin of electrons: the valence band is O 2p states, with the F⁰ and F⁺ defect states positioned in the band gap. F⁰_{HS} and F⁰_{IS} are used to denote parallel and anti-parallel alignment, respectively, of the oxygen vacancy electrons with the Mn 3d states. The energies presented are calculated with the B3LYP XC functional, and the adiabatic ionisation potential (AIP) was calculated as 1.48, 1.76 and 2.84 eV for the F⁰_{IS}, F⁰_{HS} and F⁺ defect states, respectively.

extrinsic and intrinsic defects, i.e.:



We investigated the spin-configuration explicitly by controlling the system multiplicity, with the possible spin being (a) an IS quartet or (b, c) a HS sextuplet. From the energies pre-

q	Spin	Mn _{surf}		Mn _{sub}		MgO ⁴²
		B3LYP	B97-3	B3LYP	B97-3	B3LYP
0	IS	6.16 (6.16)	5.86 (5.86)	6.13 (6.13)	5.85 (5.85)	6.59 (6.59)
1	IS	7.64 (1.49)	7.49 (1.10)	7.59 (1.44)	7.43 (1.04)	8.26 (1.80)
1	HS	7.92 (1.77)	7.75 (1.36)	7.88 (1.73)	7.71 (1.32)	-
2	IS	11.65 (-0.65)	12.24 (-0.54)	11.09 (-1.21)	11.11 (-1.67)	10.87 (-2.05)
2	HS	10.48 (-1.82)	10.38 (-2.40)	10.41 (-1.89)	10.28 (-2.50)	-

Table 4 $E_f(F^{q+})$ for the Mn-MgO (100) surface, as calculated with ϵ_f set at the vacuum (VBM) level. Both intermediate-spin (IS) and high-spin (HS) configurations were considered for $q = 1$ and 2; see the text for detailed justification. $E_f(F^{q+})$ for a low-spin MgO (100) surface are also presented from literature, with values updated using the B3LYP XC functionals, equivalent basis sets and a VBM of -6.46 eV⁴². All values are in eV.

sented in Table 4, it is clear that $E_f(F^{2+})$ is preferred in HS, with $E_f(F^{2+}) = 10.48$ and 10.41 eV for Mn_{surf} and Mn_{sub}, respectively. However, as (b) and (c) are indistinguishable by spin-state alone, comparison of the Mulliken spin populations is necessary, which shows that the spin-density on the Mn dopant is ~ 4.7 e and ~ 4.6 e for Mn_{surf} and Mn_{sub}, respectively. Thus, we can conclude that both electrons are removed from the vacancy, i.e. $V_O^\times \rightarrow V_O^{\bullet\bullet} + 2e^-$, irrespective of Mn position or XC functional. We again note that $E_f(F^{2+})$ for Mn-MgO is generally lower than for MgO, in the favoured HS state, though not when ϵ_f drops towards the VBM. Perhaps more pertinently, $E_f(F^+) > E_f(F^{2+})$ for Mn_{surf} when ϵ_f is lower than -2.84 (-2.89) eV, and F²⁺-centre formation is exothermic when ϵ_f is lower than -5.21 (-5.14) eV, i.e. p-type, when using the B3LYP (B97-3) XC functional (Figure 4).

As illustrated in Figure 5, the IS VIP for the F⁰-centre with an Mn_{surf}-dopant is found to be 2.62 eV whereas the HS VIP is 2.94 eV. Referring to our prior comment that HS corresponds to parallel alignment of the vacancy electrons and the Mn 3d states, we can re-affirm the larger $E_f(F^+)$ for a HS configuration is based on the greater stability of the highest occupied molecular orbital (HOMO) when compared to an anti-parallel (IS) configuration. The VIP of the oxygen vacancy is similar for Mn_{sub}: 2.51 and 2.92 eV for the IS and HS configuration, respectively. The upwards shift of the HOMO for an anti-parallel alignment, which is between 0.3 and 0.4 eV, gives a reasonable approximation to the exchange coupling energy, whereas the position of the parallel aligned V_O state at ~ -2.9 eV is only slightly less than the -3.05 eV calculated previously for an F⁰-centre on an MgO (100) surface.⁴² The increased stability of the parallel states is in agreement with previous observations for ferromagnetic Mn-O and Mn-C coupling in doped MgO,²⁵ though higher concentrations of Mn dopants would result in strong Mn-Mn anti-parallel coupling.^{26,30}

Using the lower energy IS F⁺-centre as our starting point, we also calculated the energy required to remove a second electron from the V_O site to form a HS F²⁺-centre. The VIP is 4.53 eV for Mn_{surf} with a very similar result of 4.52 eV

for Mn_{sub}, very close to the previously calculated 2nd VIP of an MgO F-centre (4.55 eV). Coupled with Mulliken analysis, we conclude that the second electron is also ionised from the oxygen vacancy, which means that the highest Mn 3d states must be below -4.5 eV, implying that they are stabilised by the presence of the V_O when compared to the pristine surface, for which the VIP was 4.2 to 4.4 eV (Section 4.1).

5 CO₂ Adsorption on Mn-doped MgO (100) Surface

Within the reaction process of CO₂ to CH₃OH conversion, CO₂ is bound to a surface oxygen vacancy and undergoes hydrogenation, leading to the formation of CH₃OH and the removal of the surface defect; CO is then used to regenerate the defect sites via its transformation to CO₂, completing the catalytic cycle⁷³. Such a reaction cycle is transferable and highly tunable via modification of the surface as we have recently shown for F-centres on MgO^{42,43}. As a fundamental step in this topically relevant reaction, a number of CO₂ adsorption processes were considered here for the Mn-MgO (100) surfaces investigated in Section 4. The CO₂ adsorbate was aligned with the O-C-O axis along either the Cartesian x - or z -axes of the system, “parallel” or “perpendicular” to the surface.⁴² A third CO₂ adsorbate orientation was included for Mn_{surf}, with the O-C-O axis aligned along the y -axis of the model. The adsorption energy, E_{ads} , for the CO₂ molecule was defined as:

$$E_{ads}(CO_2) = E(CO_2\text{-MnMgO}) - E(CO_2) - E(\text{MnMgO}), \quad (16)$$

where $E(CO_2)$ and $E(CO_2\text{-MnMgO})$ are the energies of the gas phase CO₂ and Mn-MgO adsorbed CO₂ systems, respectively. Energetic errors from basis set superposition were not explicitly calculated; however we expect them to be similar to the quantity calculated previously for CO₂ chemisorbed on MgO (0.15 - 0.18 eV).⁴² A HS configuration was considered for the O_{5c} site and F²⁺ defects, with the F⁰ defects modelled

using the lower-energy IS configuration, and both IS and HS configurations investigated for F^+ -centres. We note that the CO_2 molecule has a closed-shell (singlet) electronic configuration in the gas-phase and so electron transfer to an adsorbed CO_2 could be in to either the α - or β -channels with equal probability. At this stage, we have limited our investigation to the determination of adsorbed structures and analysis of any electron transfer, with adsorption profiles and barriers reserved for future work.

5.1 O_{5c} Site

The adsorbed structures for CO_2 parallel to the Mn_{surf} -MgO (100) surface are shown in Figures 6 (a) and (b), whilst CO_2 adsorption parallel to the Mn_{sub} -MgO surface is shown in Figure 6 (c). The CO_2 adsorbate perpendicular to the O_{5c} site is not shown as significant interactions were not seen: this was expected, based on previous results for MgO,⁴² and the data presented in the Supplementary Information (SI) shows that the interaction is negligible. In experiment, Van der Waals interactions that are absent from our calculations would perhaps allow the CO_2 to be stabilised near the Mn-MgO surface.

For the x - and y -axis aligned adsorbates, a pseudo-carbonate species forms and $E_{ads}(CO_2)$ on the O_{5c} site ranges between -0.66 and -0.86 eV, which is similar to that observed for MgO⁴²; full results are included in the SI. We note for Mn_{surf} that stronger CO_2 adsorption is seen for y -axis alignment, compared to x -axis, which can be correlated with the longer Mn-O bond of 2.29 Å between the (100) surface and the CO_2 in the latter system. Mulliken analysis shows that there is partial withdrawal of ~ 0.5 e from the O_{5c} and neighbouring Mg atoms to the adsorbate; however the Mn-dopant retains its d^5 configuration and this hinders charge transfer.

Comparison of the different XC functionals shows consistently stronger binding when using B97-3, with the interactions around 10% stronger than for B3LYP. This result is consistent with the parameterisation of this XC functional towards thermochemical processes such as chemisorption.

5.2 F^0 -Centre

For a neutral oxygen vacancy, the z -axis (vertically) aligned CO_2 dissociates to produce a defect-free surface and a CO molecule, as shown in Figure 7(a). Table 5 shows that this process is strongly exothermic (~ -3 eV) due to the healing of the oxygen vacancy. Strong adsorption also occurs when CO_2 is aligned parallel to the surface, with $E_{ads}(CO_2) \approx -2$ eV. The strong binding results in a bent CO_2 geometry, as seen previously for F^0 -centre on MgO,⁴² however healing of the oxygen vacancy does not occur in this particular case. The structural changes observed are accompanied by a transfer of electron density from the Mg atoms to the CO_2 ; the Mn^{2+} cation does

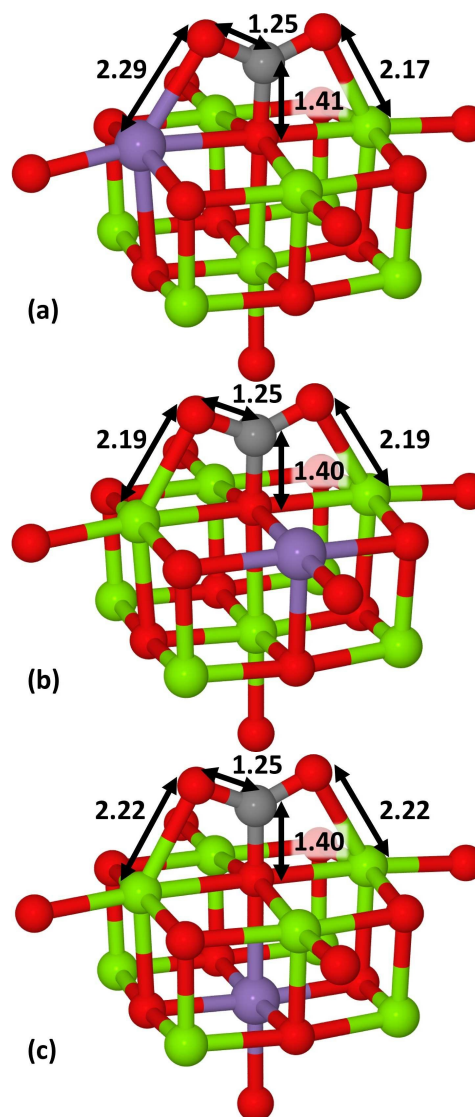


Fig. 6 CO_2 adsorbed on the Mn-MgO (100) surface, where the CO_2 molecule is adsorbed in the xy - surface plane. In (a) and (b), the CO_2 molecule is positioned in the x - and y -axes, respectively, over an Mn_{surf} -MgO substrate; In (c), the CO_2 molecule is adsorbed over an Mn_{sub} -MgO substrate. O atoms are shown in red, Mg in green, Mn in purple and C in grey. Bond lengths are given in Å.

not contribute. Regardless of the position of the Mn dopant, the CO_2 rotates so that the central C atom is directed towards a surface Mg, rather than downwards into the vacancy as seen for undoped MgO.⁴² It is noted that, in the y -axis orientation on Mn_{surf} -MgO, the CO_2 is able to rotate towards either an Mn or Mg atom, however the latter is favoured.

	CO ₂ axis	B3LYP	B97-3
Mn _{surf}	x	-2.00	-1.74
	y	-2.25	-1.98
	z	-3.13	-2.80
Mn _{sub}	x	-2.24	-1.98
	z	-3.20	-2.87
Mg ⁴²	x	-2.36	-
	z	-3.52	-

Table 5 $E_{ads}(\text{CO}_2)$ on F^0 -centres at the (100) surface. Also presented are previously calculated results for CO_2 adsorption on MgO using the B3LYP XC functional and similar basis sets.⁴² All values are given in eV.

5.3 F^+ -Centre

Due to the energetic competition between the IS and HS F^+ -centres, both were considered as adsorption sites for CO_2 (Table 6), which resulted in a range of adsorption strengths. $E_{ads}(\text{CO}_2)$ is greatest for IS Mn_{surf}-MgO with the adsorbate aligned along the x -axis of the surface (-2.00 eV). Figure 8(a) shows that the CO_2 has dissociated, with one O healing the surface vacancy and the remaining CO coordinated to a surface Mg. Mulliken analysis shows that the electron previously trapped at the F^+ -centre has reduced the Mn^{2+} cation to Mn^+ , which has a spin-density to 3.90 e. For the same system with a HS configuration, no dissociation is observed and instead the vacancy-trapped electron transfers to the CO_2 , hence the smaller $E_{ads}(\text{CO}_2)$. The second greatest $E_{ads}(\text{CO}_2)$ is with the CO_2 aligned in the y -axis of an IS-configured surface (-1.38 eV): the CO_2 remains parallel to the surface but the C bonds directly to the Mn, with the two atoms separated by 2.14 Å compared to 2.61 Å for the HS equivalent as shown in Figures 8(c) and (d), respectively. The spin-density is 4.08 e in the former case, which is ~ 0.7 e lower than for HS (4.76 e) and again indicates that the vacancy electron has moved to the Mn.

In contrast to the above, $E_{ads}(\text{CO}_2)$ for z -axis aligned CO_2 on the Mn_{surf} is stronger for HS than IS, with no chemisorption, which indicates that exchange coupling benefits physisorption. The resulting bent CO_2 remains perpendicular to the surface for both systems [Figures 8(e) and (f)], with the terminal O only ~ 0.7 Å above the surface plane, but the difference in $E_{ads}(\text{CO}_2)$ between HS and IS is 0.22 eV. Similar differences are seen for the Mn_{sub} systems [Figure 7(b)], where $E_{ads}(\text{CO}_2)$ for HS is consistently ~ 0.2 eV greater than for IS. Mulliken analysis of the CO_2 when x -axis aligned on Mn_{sub}-MgO shows that the spin-density is 0.69 and 0.84 e when using IS and HS configurations, respectively, which correlates charge transfer with adsorption energy; we also note that the majority of this spin density is located on the central C atom.

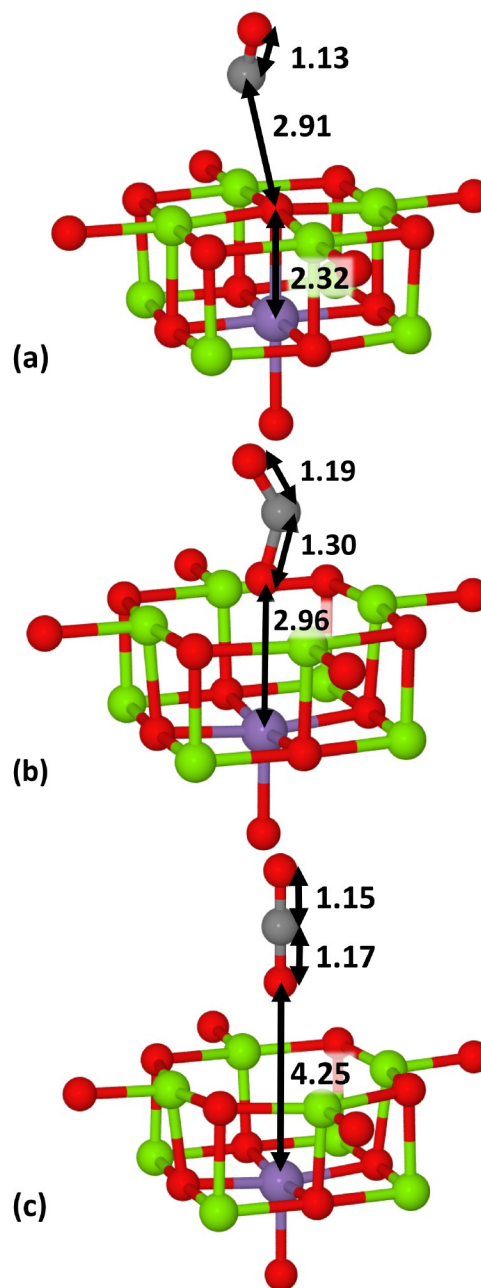


Fig. 7 CO_2 adsorbed on the Mn_{sub}-MgO(100) surface at an (a) F^0 -Centre, (b) F^+ -Centre and (c) F^{2+} -Centre. O atoms are shown in red, Mg in green, Mn in purple and C in grey. Bond lengths are given in Å

5.4 F^{2+} -Centre

$E_{ads}(\text{CO}_2)$ on HS F^{2+} -centres is presented in Table 7, with similar structures observed for CO_2 adsorbed on Mn_{sub}- and Mn_{surf}-MgO [Figure 7(c)]. Bonding is marginally exothermic for z -axis aligned CO_2 , with the lack of bend in the adsorbate

	CO ₂ axis	B3LYP	B97-3
Mn _{surf}	x	-2.00 (-0.62)	-1.64 (-0.48)
	y	-1.38 (-0.80)	-1.06 (-0.64)
	z	-0.90 (-1.12)	-0.76 (-0.97)
Mn _{sub}	x	-0.64 (-0.85)	-0.49 (-0.69)
	z	-0.99 (-1.18)	-0.85 (-1.05)
Mg ⁴²	x	-0.71	-
	z	-1.11	-

Table 6 $E_{ads}(\text{CO}_2)$ on F^{+} -centre sites, with an IS (HS) electronic configuration, on Mn-MgO (100) surface. Also presented are previously calculated results for CO_2 adsorption on MgO using the B3LYP XC functional and similar basis sets.⁴² All values are given in eV.

	CO ₂ axis	B3LYP	B97-3
Mn _{surf}	x	0.90	1.14
	y	0.50	0.00
	z	-0.09	-0.11
Mn _{sub}	x	0.24	0.52
	z	-0.12	-0.13
Mg ⁴²	x	0.11	-
	z	0.04	-

Table 7 $E_{ads}(\text{CO}_2)$ on F^{2+} -centres. Also presented are previously calculated results for CO_2 adsorption on MgO using the B3LYP XC functional and similar basis sets.⁴² All values are given in eV.

suggesting that no significant charge transfer occurs, which is consistent with results for undoped MgO^{42} and confirmed by Mulliken analysis. CO_2 adsorption is endothermic when the molecule is aligned with the x - or y -axis; as separation of the CO_2 and surface would be more favourable, this is a local minimum. Electron density transfers from the Mn atom to the CO_2 to form a $\text{CO}_2^-/\text{Mn}^{3+}$ surface complex, with greater charge transfer when the Mn interacts with a terminal O (x -axis) rather than the C atom (y -axis), which correlates with the more endothermic nature of the x -axis aligned adsorption (0.90 eV compared to 0.50 eV).

6 Summary and Conclusions

We have performed embedded-cluster QM/MM calculations for Mn-doped MgO, studying bulk and (100) surface systems, as well as testing the reactivity of the doped material using CO_2 adsorption as a representative catalytic process. Low concentration Mn-doping is endothermic for isovalent bulk defects, irrespective of a low or high $p(\text{O}_2)$ reference environment, with the Mn 3d levels positioned in the band gap ~ 4.2

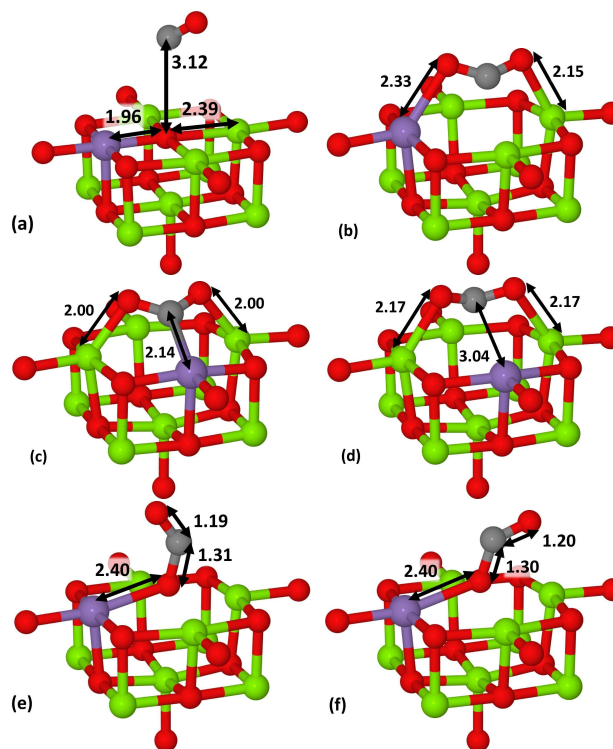


Fig. 8 CO_2 adsorbed on the Mn_{surf}-MgO(100) surface at an F^{+} -Centre with the adsorbate aligned (a, b) in the x -axis, (c, d) in the y -axis, and (e, f) in the z -axis. Figures (a), (c) and (e) are with anti-parallel spin for the vacancy and the Mn 3d states, i.e. IS configuration, and (b), (d) and (f) are parallel spin for the vacancy and the Mn 3d states, i.e. HS configuration. O atoms are shown in red, Mg in green, Mn in purple and C in grey. Bond lengths are given in Å

eV below the vacuum level, however, Mn-doping is energetically favourable in higher oxidation states, especially under p -type conditions. The formation of isovalent Mn-doped (100) MgO surfaces is marginally exothermic at high $p(\text{O}_2)$, with subsurface doping endothermic, however higher oxidation states become more favourable in p -type conditions.

Once present, an isovalent Mn-dopant aids the formation of oxygen vacancies, i.e. F-centres, on the (100) surface: F^{+} -centres particularly benefit from an exchange-coupling mechanism between the trapped electrons and the Mn 3d-states, with a parallel aligned electron 0.32 eV lower in energy than an anti-parallel aligned electron when using the B3LYP XC functional. In general, formation energies for F^0 and F^{2+} -centres indicate their prevalence in n - and p -type environments, respectively, in broad agreement with MgO; in future work we will extend this analysis to Mn-dopants in higher oxidation states.

When a CO_2 probe molecule is adsorbed on the pristine and defective Mn-MgO (100) surface, the interaction between

substrate and adsorbate is dependent on both defect charge and adsorbate orientation. Strongest adsorption is for CO₂ over an F⁰-centre, with the CO₂ dissociating when aligned perpendicular to the surface so that the oxygen vacancy can be filled by one of the oxygen atoms from the CO₂ molecule. We also observe strong binding between F⁺-centres and CO₂ when the Mn-dopant is positioned at the surface, with interaction strengths less varied when the Mn is subsurface. In general, positioning of an Mn-dopant subsurface implicitly affects CO₂ adsorption through exchange coupling effects, whereas Mn dopants on the surface strongly influence the chemical reactivity, with distinctly different interactions compared to MgO. In general our results justify further investigation of the doping of stable alkaline-earth metal oxides with transition metal species, which we will continue in our future work with an emphasis on catalytic reactivity: it has been previously noted that high-valence dopants activate molecular adsorbates for other transition metal dopants in rocksalt oxides⁷⁸ and clearly we need to investigate this further for Mn-MgO.

7 Acknowledgements

The authors are grateful to David Scanlon and John Buckridge for discussions associated with this work. AJL acknowledges the Ramsay Memorial Trust and University College London for the provision of a Ramsay Fellowship. CAD acknowledges the Molecular Modelling and Materials Science Industrial Doctorate Centre (M3S IDC) and the Science and Technology Facilities Council (STFC) for funding. AJL, TWK, PS, AAS and CRAC acknowledge funding from EPSRC grants EP/IO30662/1 and EP/K038419/1. The authors acknowledge the use of the ARCHER high-performance computing facilities, and associated support services, via our membership of the UK HPC Materials Chemistry Consortium (EP/L000202).

References

- S. Wang, S. Yan, X. Ma and J. Gong, *Energy Environ. Sci.*, 2011, **4**, 3805–3819.
- S. Choi, J. H. Drese and C. W. Jones, *ChemSusChem*, 2009, **2**, 796–854.
- H. A. Al-Abadleh and V. H. Grassian, *Surf. Sci. Rep.*, 2003, **52**, 63–161.
- D. P. Woodruff, *Chem. Rev.*, 2013, **113**, 3863–3886.
- C. Noguera, *Physics and Chemistry at Oxide Surfaces*, Cambridge University Press, 1996.
- A. J. Logsdail, D. O. Scanlon, C. R. A. Catlow and A. A. Sokol, *Phys. Rev. B*, 2014, **90**, 155106.
- A. J. Logsdail, D. Mora-Fonz, D. O. Scanlon, C. R. A. Catlow and A. A. Sokol, *Surf. Sci.*, 2015, **642**, 58–65.
- G. Pacchioni, *ChemPhysChem*, 2003, **4**, 1041–1047.
- K. Honkala, *Surf. Sci. Rep.*, 2014, **69**, 366–388.
- H. Hattori, *Appl. Catal. A: Gen.*, 2001, **222**, 247–259.
- J. Goniakowski and C. Noguera, *Surf. Sci.*, 1995, **340**, 191–204.
- G. Pacchioni and H. Freund, *Chem. Rev.*, 2013, **113**, 4035–4072.
- D. K. Kanan and E. A. Carter, *J. Phys. Chem. C*, 2012, **116**, 9876–9887.
- R. Hammami, A. Dhoubib, S. Fernandez and C. Minot, *CATALYSIS TODAY*, 2008, **139**, 227–233.
- N. Nilius and H.-J. Freund, *Accounts of Chemical Research*, 2015, **48**, 1532–1539.
- E. W. McFarland and H. Metiu, *Chemical Reviews*, 2013, **113**, 4391–4427.
- N. Nilius, *Journal of Physics: Condensed Matter*, 2015, **27**, 303001.
- A. Cimino and V. Indovina, *Journal of Catalysis*, 1974, **33**, 493–496.
- P. Koidl and K. W. Blazey, *J. Phys. C: Solid State Phys.*, 1976, **9**, L167.
- R. Mariscal, J. Soria, M. Pena and J. Fierro, *J. Catal.*, 1994, **147**, 535–543.
- M. Abramishvili, Z. Akhvediani, M. Galustashvili, G. Dekanozishvili, T. Kalabegishvili, V. Kvachadze and V. Tavkhelidze, *J. Mod. Phys.*, 2011, **2011**, year.
- M. Königstein, F. Cora and C. R. A. Catlow, *Journal of Solid State Chemistry*, 1998, **137**, 261–275.
- H. Gripenberg, S. Seetharaman and L. Staffansson, *Chemica Scripta*, 1979, **13**, 162–164.
- K. D. Heath, W. C. Mackrodt, V. R. Saunders and M. Causà, *Journal of Materials Chemistry*, 1994, **4**, 825–829.
- V. Sharma, G. Pilania and J. E. Lowther, *AIP Adv.*, 2011, **1**, 032129.
- L.-J. Shi, *Phys. Lett. A*, 2010, **374**, 1292–1296.
- S. Azzaza, M. El-Hilo, S. Narayanan, J. J. Vijaya, N. Mamouni, A. Benyoussef, A. El Kenz and M. Bououdina, *Mater. Chem. Phys.*, 2014, **143**, 1500–1507.
- S. Meskine, A. Boukortt, R. Hayn and A. Zaoui, *Phys. Status Solidi B*, 2014, **251**, 845–849.
- P. Wu, G. Cao, F. Tang and M. Huang, *Comp. Mater. Sci.*, 2014, **86**, 180–185.
- P. Panigrahi, T. Hussain, C. M. Araujo and R. Ahuja, *J. Phys.: Condens. Matter*, 2014, **26**, 265801.
- P. Panigrahi, C. M. Araujo, T. Hussain and R. Ahuja, *Sci. Technol. Adv. Mater.*, 2014, **15**, 035008.
- N. A. Richter, S. Siculo, S. V. Levchenko, J. Sauer and M. Scheffler, *Phys. Rev. Lett.*, 2013, **111**, 045502.
- F. Kröger and H. Vink, *H. Vink*, Academic Press, 1956, vol. 3, pp. 307–435.
- E. Scorza, U. Birkenheuer and C. Pisani, *J. Chem. Phys.*, 1997, **107**, 9645–9658.
- P. V. Sushko, A. L. Shluger and C. R. A. Catlow, *Surf. Sci.*, 2000, **450**, 153–170.
- P. Sushko, J. Gavartin and A. Shluger, *J. Phys. Chem. B*, 2002, **106**, 2269–2276.
- Y. Wang, H. N. Nguyen and T. N. Truong, *Chem.-Eur. J.*, 2006, **12**, 5859–5867.
- E. Florez, P. Fuentealba and F. Mondragon, *Catal. Today*, 2008, **133**, 216–222.
- C. Qin, *Chem. Phys. Lett.*, 2008, **460**, 457–460.
- G. Pacchioni and H.-J. Freund, *Chem. Rev.*, 2013, **113**, 4035–4072.
- K. Kwapien, J. Paier, J. Sauer, M. Geske, U. Zavyalova, R. Horn, P. Schwach, A. Trunschke and R. Schlögl, *Angew. Chem. Int. Ed.*, 2014, **53**, 8774–8778.
- C. A. Downing, A. A. Sokol and C. R. A. Catlow, *Phys. Chem. Chem. Phys.*, 2014, **16**, 184–195.
- C. A. Downing, A. A. Sokol and C. R. A. Catlow, *Phys. Chem. Chem. Phys.*, 2014, **16**, 21153–21156.
- S. Metz, J. Kästner, A. A. Sokol, T. W. Keal and P. Sherwood, *WIREs Comput Mol Sci*, 2014, **4**, 101–110.
- J. Kaestner, J. M. Carr, T. W. Keal, W. Thiel, A. Wander and P. Sherwood, *J. Phys. Chem. A*, 2009, **113**, 11856–11865.
- P. Sherwood, A. H. de Vries, M. F. Guest, G. Schreckenbach, C. R. A. Catlow, S. A. French, A. A. Sokol, S. T. Bromley, W. Thiel, A. J. Turner, S. Billeter, F. Terstegen, S. Thiel, J. Kendrick, S. C. Rogers, J. Casci, M. Watson, F. King, E. Karlsen, M. Sjøvoll, A. Fahmi, A. Schafer and

- C. Lennartz, *Theochem-J. Mol. Struct.*, 2003, **632**, 1–28.
- 47 M. Valiev, E. J. Bylaska, N. Govind, K. Kowalski, T. P. Straatsma, H. J. J. V. Dam, D. Wang, J. Nieplocha, E. Apra, T. L. Windus and W. A. de Jong, *Comput. Phys. Commun.*, 2010, **181**, 1477–1489.
- 48 J. D. Gale, *J. Chem. Soc.-Faraday Trans.*, 1997, **93**, 629–637.
- 49 J. D. Gale and A. L. Rohl, *Mol. Simul.*, 2003, **29**, 291–341.
- 50 J. Gale, *Z. Kristall.*, 2005, **220**, 552–554.
- 51 A. D. Becke, *J. Chem. Phys.*, 1993, **98**, 5648–5652.
- 52 C. T. Lee, W. T. Yang and R. G. Parr, *Phys. Rev. B*, 1988, **37**, 785–789.
- 53 P. J. Stephens, F. J. Devlin, C. F. Chabrowski and M. J. Frisch, *J. Phys. Chem.*, 1994, **98**, 11623–11627.
- 54 T. W. Keal and D. J. Tozer, *J. Chem. Phys.*, 2005, **123**, 121103.
- 55 F. Weigend and R. Ahlrichs, *Phys. Chem. Chem. Phys.*, 2005, **7**, 3297–3305.
- 56 M. Dolf, U. Wedig, H. Stoll and H. Preuss, *J. Chem. Phys.*, 1987, **86**, 866–872.
- 57 P. Fuentealba, L. Vonszentpaly, H. Preuss and H. Stoll, *J. Phys. B-At. Mol. Opt. Phys.*, 1985, **18**, 1287–1296.
- 58 G. V. Lewis and C. R. A. Catlow, *J. Phys. C*, 1985, **18**, 1149–1161.
- 59 W. Jost, *J. Chem. Phys.*, 1933, **1**, 466–475.
- 60 A. E. Hughes and B. Henderson, in *Point Defects in Solids: General and Ionic Crystals*, ed. J. H. Crawford and L. M. Slifkin, Springer US, Boston, MA, 1972, ch. Color Centers in Simple Oxides, pp. 381–490.
- 61 F. Stavale, X. Shao, N. Nilius, H.-J. Freund, S. Prada, L. Giordano and G. Pacchioni, *Journal of the American Chemical Society*, 2012, **134**, 11380–11383.
- 62 Y. Cui, X. Shao, S. Prada, L. Giordano, G. Pacchioni, H.-J. Freund and N. Nilius, *Phys. Chem. Chem. Phys.*, 2014, **16**, 12764–12772.
- 63 A. Walsh, J. Buckeridge, C. R. A. Catlow, A. J. Jackson, T. W. Keal, M. Miskufova, P. Sherwood, S. A. Shevlin, M. B. Watkins, S. M. Woodley and A. A. Sokol, *Chemistry of Materials*, 2013, **25**, 2924–2926.
- 64 D. R. Lide, *CRC Handbook of Chemistry and Physics, 84th Edition*, CRC Press, Boca Raton, Florida, 2003.
- 65 J. P. Perdew, K. Burke and M. Ernzerhof, *Phys. Rev. Lett.*, 1996, **77**, 3865–3868.
- 66 R. O. Jones and O. Gunnarsson, *Rev. Mod. Phys.*, 1989, **61**, 689–746.
- 67 T. Jaouen, G. Jézéquel, G. Delhaye, B. Lépine, P. Turban and P. Schieffer, *Appl. Phys. Lett.*, 2010, **97**, 232104.
- 68 R. Whited, C. J. Flaten and W. C. Walker, *Solid State Commun.*, 1973, **13**, 1903–1905.
- 69 R. D. Shannon, *Acta. Cryst.*, 1976, **32**, 751–767.
- 70 L. N. Kantorovich, A. L. Shluger, P. V. Sushko, J. Gunster, P. Stracke, D. W. Goodman and V. Kempter, *Faraday Discuss.*, 1999, **114**, 173–194.
- 71 H. H. Kung, *Transition metal oxides: surface chemistry and catalysis*, Elsevier, 1989, vol. 45.
- 72 D. O. Scanlon, C. W. Dunnill, J. Buckeridge, S. A. Shevlin, A. J. Logsdail, S. M. Woodley, C. R. A. Catlow, M. J. Powell, R. G. Palgrave, I. P. Parkin, G. W. Watson, T. W. Keal, P. Sherwood, A. Walsh and A. A. Sokol, *Nature Mater.*, 2013, **12**, 798–801.
- 73 S. A. French, A. A. Sokol, S. T. Bromley, C. R. A. Catlow, S. C. Rogers, F. King and P. Sherwood, *Angew. Chem.-Int. Edit.*, 2001, **40**, 4437–4440.
- 74 A. Sokol, S. Bromley, S. French, C. Catlow and P. Sherwood, *Int. J. Quantum Chem.*, 2004, **99**, 695–712.
- 75 S. French, A. Sokol, S. Bromley, C. Catlow and P. Sherwood, *Top. Catal.*, 2003, **24**, 161–172.
- 76 S. Bromley, S. French, A. Sokol, C. Catlow and P. Sherwood, *J. Phys. Chem. B*, 2003, **107**, 7045–7057.
- 77 C. Catlow, S. French, A. Sokol and J. Thomas, *Philos. Trans. R. Soc. A-Math. Phys. Eng. Sci.*, 2005, **363**, 913–936.
- 78 Y. Cui, X. Shao, M. Baldofski, J. Sauer, N. Nilius and H.-J. Freund, *Angewandte Chemie International Edition*, 2013, **52**, 11385–11387.